Liquid mediated growth and the bimodal microstructure of $YBa_2Cu_3O_{7-\delta}$ films made by the ex situ conversion of physical vapor deposited BaF_2 precursors

T.G. Holesinger[a] and P.N. Arendt
Los Alamos National Laboratory, Los Alamos, New Mexico 87545

R. Feenstra, A.A. Gapud, and E.D. Specht
Oak Ridge National Laboratory, Oak Ridge, Tennessee 37831

D.M. Feldmann and D.C. Larbalestier
University of Wisconsin, Madison, Wisconsin 53706

(Received 3 August 2004; accepted 7 February 2005)

$YBa_2Cu_3O_y$ (YBCO) films produced by the ex situ conversion of BaF_2-based precursors deposited by physical vapor deposition on ion-beam assisted deposited (IBAD) yttrium-stabilized zirconia (YSZ) and rolling-assisted biaxially textured substrates (RABiTS) templates are characterized by a bi-axially aligned, laminar grain structure that results from the anisotropic growth characteristics of the YBCO phase and its precipitation from a transient liquid phase during the conversion process. A bimodal microstructure characterizes these films and is defined by large, well-formed YBCO grains with Y_2O_3 precipitates in the bottom region of the film and small YBCO grains with a high density of stacking faults in the upper half. $Ba_2Cu_3O_y$ or Ba–O–F/CuO second phase layers were often found between large YBCO grains in the bottom half of the films. YBCO grain sizes exceeded 50 μm within the plane of the film in some cases. Conversely, discrete secondary phases of $Y_2Cu_2O_5$, Y_2O_3, and $Ba_2Cu_3O_y$/Ba–O–F could be found among the much smaller YBCO grains in the top portion of the bimodal structure. The dividing line of the bimodal structure was generally at one half of the film thickness, although exceptions to this trend were found. The highest critical current densities (J_c) and best film alignments for a given film thickness were found in samples where the layers of $Ba_2Cu_3O_y$ or Ba–O–F were minimized or eliminated from the films. Samples quenched after partial conversion show the segregation of CuO to the top region of the film and the lateral growth of large YBCO grains from a precursor mix of $Y_2Cu_2O_5$ and Ba–O–F. The data demonstrate that transient liquid phases are part of the conversion process of BaF_2-based YBCO films. The control of both CuO segregation and the amount of liquid phases generated during the initial stages of phase formation is needed for optimizing the ex situ conversion process for high-J_c coated conductors.

I. INTRODUCTION

Two key areas for commercial development of coated conductors are the production of suitable long-length, textured templates and the development of high-rate, high-quality epitaxial deposition processes for buffer and $YBa_2Cu_3O_y$ (YBCO) layers.[1] YBCO-coated conductors are based on the epitaxial deposition of buffer layers and YBCO onto bi-axially textured templates.[2–10] The manufacture of the composite is an aggregate process built on the layering of functional metal or metal oxide layers onto the textured substrate; the superconducting YBCO film is but one of the layers in the composite. The YBCO film is typically the thickest of the oxide layers. Because of the constraints imposed by even low-angle YBCO misorientations,[11–13] the polycrystalline YBCO films need single-crystal-like properties with respect to their textures and grain-to-grain connectivity.

Coating technologies for large-scale production of YBCO-coated conductors will require processes with high rates of deposition and large deposition areas. The number of suitable processes for YBCO deposition is further limited by the requirement of high critical currents (I_c) in excess of 200–300 A/(cm width) of conductor. This level of I_c performance is currently available in

[a]Address all corrrespondence to this author.
e-mail: holesinger@lanl.gov
DOI: 10.1557.JMR/2005.0150

production $(Bi,Pb)_2Sr_2Ca_2Cu_3O_y$ (Bi-2223) powder-in-tube tapes, which YBCO-coated conductors are expected to replace.[14] This I_c performance level will most likely be obtained only through thick films ($\geq$1 μm) of YBCO where the critical current density (J_c) of the YBCO films is in excess of 1 MA/cm^2 at liquid-nitrogen temperatures and self-field. Examples of some processes that can meet these requirements are ex situ conversion of YBCO precursors,[15–23] metalorganic chemical vapor deposition (MOCVD),[24,25] and physical vapor deposition (PVD) from mixed oxide targets or elemental sources in a suitable oxidizing vacuum environment.[26–31]

The ex situ conversion of BaF_2-based $YBa_2Cu_3O_y$ precursors is an economically attractive process for adding the superconducting layer to a coated conductor substrate. Understanding the phase conversion process and final microstructural assemblage is crucial to maximizing the superconducting properties. The deposition of the BaF_2-based precursors can be carried out by one of two methods. The first process, as first described by Mankiewich et al., is the physical vapor deposition (PVD) of Y metal, BaF_2, and Cu metal onto a suitably buffered template and is referred to as the PVD-BaF_2 process.[32] PVD-BaF_2 processes are of interest because one can easily fabricate YBCO films up to 5 μm or more in thickness. The related method first demonstrated by Gupta et al. is based on the metalorganic deposition (MOD) of trifluoroactetate precursors and is referred to as the MOD-BaF_2 process.[15] Both processes have the capacity for producing high critical current density (J_c) YBCO films at high conversion rates.[9,19–21,23,33] The conversion processes for the MOD-BaF_2 and PVD-BaF_2 precursor films share many key features after the pyrolysis step that converts the MOD-BaF_2 TFA-based precursors into the mixed metal oxyfluorides.[15,34] Areas of particular interest in the processing of BaF_2-based YBCO films are nucleation and growth[16,18,35,36] in the presence of transient liquid phases,[16,18,35] rate limiting mechanisms,[37,38] oxygen partial pressures during processing,[16,17] through thickness J_c uniformity,[39] and residual porosity in ex situ films.[34,40]

This paper focuses on the microstructural development in thick YBCO films made by ex situ conversion of PVD-BaF_2 precursors. An effort is made to characterize the typical features of these high-J_c films, correlate the presence of a transient liquid phase to the microstructural development and properties of the YBCO films, and correlate film structure with transport properties with the goal of identifying key current limiting microstructures.

II. EXPERIMENTAL

The samples examined in this study consisted of coated conductors with YBCO films made by the physical vapor deposition of metal and fluoride precursors (PVD-BaF_2) onto a suitable template followed by an ex situ conversion process.[17] The YBCO precursors, Y metal, BaF_2, and Cu metal, were deposited by electron beam evaporation in a vacuum system. The films were subsequently removed and placed in a furnace operated at atmospheric pressures for the conversion heat treatment. The samples were processed using a two-step anneal consisting of a nucleation step at 750 °C with reduced water supply [p(H_2O) < 1 Torr], followed by a "growth" step at 780 °C with p(H_2O) ≈ 3 to 4 Torr. During the nucleation step, an epitaxially aligned layer of YBCO is believed to form along the interface with the buffer layer. Insertion of the reduced water supply nucleation step to enhance *c*-axis growth is similar to that described by Smith et al.[19] for thick MOD-derived films. The average growth rate of the YBCO over the nucleation and growth steps combined is about 1 Å/s. The oxygen partial pressure throughout the entire conversion process was kept at 0.2 Torr. Further details of the processing are described elsewhere.[41] Typical sample dimensions were 1.5 × 0.5 cm. Most of the PVD-BaF_2 films were deposited on NiW rolling-assisted biaxially textured substrates (RABiTS). For comparison, a few PVD-BaF_2 films were made on ion-beam-assisted deposition (IBAD) yttria-stabilized zirconia (YSZ) templates on polycrystalline Hastelloy substrates. The RABiTS-based coated conductors had a typical architecture of YBCO/CeO_2 (15 nm)/YSZ (150 nm)/Y_2O_3 (20 nm)/Ni (1500 nm)/RABiTS NiW(3 at.%). The IBAD YSZ-based composites had an architecture of YBCO/CeO_2/IBAD YSZ/Hastelloy. Additional details of the processing of RABiTS templates and IBAD YSZ templates can be found in the literature.[7,42] For brevity, samples referred to as RABiTS or IBAD YSZ samples in the text will be understood to include the textured template plus the buffer or YBCO layers described above, respectively.

Because the samples are cut either perpendicular or parallel to the long axis of the metal composite tapes, the YBCO films in the cross sections are always viewed along a {100}-type direction. This is not immediately clear as one or more 45° rotations are often produced during epitaxial oxide deposition on the starting metal tapes. Figure 1 shows schematics of the cross sections and in-plane alignments and rotations of the differing layers in the composites. The RABiTS template is textured with the Ni ⟨100⟩ aligned with the rolling direction or long axis of the tape.[7] The metaloxide epitaxy of the Y_2O_3 seed layer results in a 45° in-plane rotation for the Y_2O_3 ⟨100⟩.[43] The YSZ and CeO_2 layers added to the composite repeat the orientation of the Y_2O_3. During the processing of an IBAD YSZ tape, the YSZ oxide layer aligns with the ⟨100 ⟩ direction rotated 45° from the long axis of the polycrystalline Ni-alloy tape.[42] The CeO_2 cap aligns cube-on-cube with the IBAD YSZ layer. At this point, the orientations of the CeO_2 layers on the RABiTS and IBAD YSZ samples are equivalent with respect to

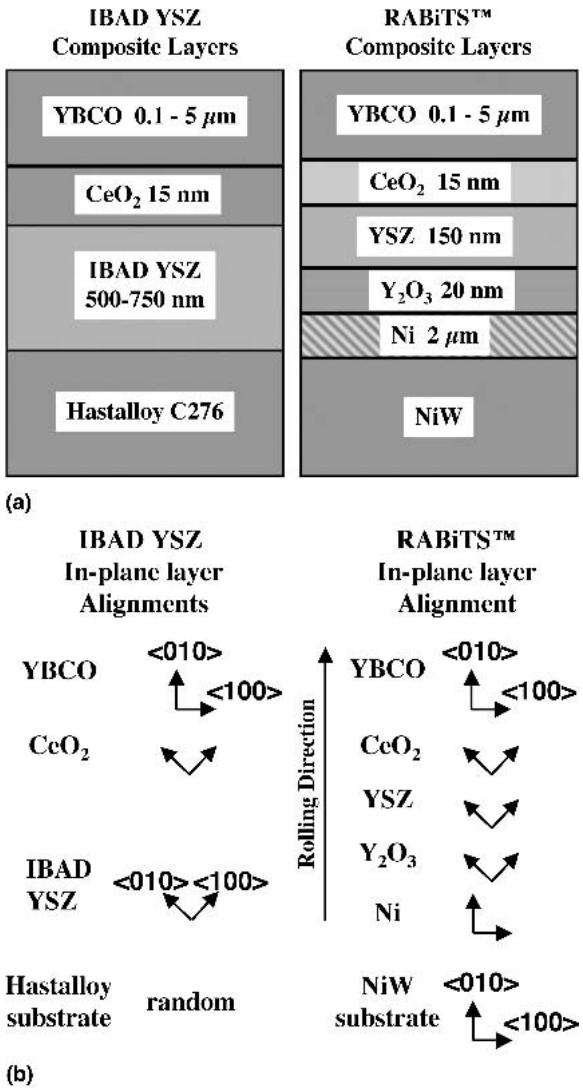

FIG. 1. (a) Architectures viewed in cross-section of the RABiTS and IBAD YSZ composites examined in this work and (b) the crystallographic orientations and indicated rotations viewed in plan view of the individual buffer layers relative to the rolling directions of the substrates. In both cases, the YBCO ⟨100⟩ is aligned parallel to the rolling direction of the substrates. Note that the IBAD YSZ layer is rotated 45° to the rolling direction of the substrate due to the deposition conditions needed to produce the textured film.

the rolling directions of the tapes. The deposition of the YBCO on the CeO_2 cap layers results in one more 45° rotation and aligns the YBCO ⟨100⟩ with the long axes of the tapes.

Cross-sectional and plan-view scanning, transmission, and scanning transmission electron microscopy (SEM, TEM, and STEM) were used to obtain multiple views of the BaF_2-based YBCO films on RABiTS and IBAD YSZ templates. Multiple methods were used to prepare specimens for SEM, TEM, and STEM. With the conventional cross-sectional method, samples were cut and glued between two pieces of silicon. The samples were then mounted in 3-mm non-magnetic stainless steel tubes, sliced, dimple-polished, and then ion-milled to electron transparency. Samples were prepared for plan-view TEM by cutting 3-mm disks from the conductors, thinning the disks down to 40 μm from the backside, dimple-polishing the backside, and then ion-milling to electron transparency. In a few cases, TEM specimens were prepared with the use of a focused ion beam (FIB). A slice of approximate dimensions 20 × 7 × 1 μm was cut with the FIB from a sample, welded to a Cu grid in situ, and then thinned and polished to electron transparency with the ion beam.

Phase identification was performed by energy dispersive spectroscopy (EDS) and electron diffraction. In some instances, quantitative analysis of secondary phases was performed with the Cliff–Lorimer approach using the Y-123 grains in the film as an internal standard.[44] Fully processed coated conductors were additionally characterized by x-ray diffraction for the in-plane and out-of-plane alignments and measurement of the transition temperature (T_c) and critical current (I_c) at liquid-nitrogen temperatures (77 K). Transport critical currents were in most cases measured across the full width of the samples at 0.3 T and are reported in A/cm width. Measurement in field was undertaken to avoid sample burnout that occurs with short samples and high currents, although in a few cases, self-field measurements were made. Critical current densities (J_c) at 77 K and self-field on RABiTS were calculated by multiplying the 0.3T J_c values by 3.2. The latter value was derived by determining the difference of the self-field and 0.3 T J_c values from a set of 0.35-μm-thick YBCO films.

Characterization of the average in-plane and out-of-plane alignment was accomplished by x-ray diffraction (XRD) using a four-circle diffractometer and Cu K_α radiation. Rocking curves (ω scans) and ϕ scans were fit to Gaussian lineshapes, for which the full widths at half maximum (FWHM) are reported. Out-of-plane mosaic is measured by YSZ(002) and YBCO(006) rocking curves. Rocking curves are taken with the axis of rotation parallel first to the cross direction (which gives the narrower mosaic spread for RABiTS substrates) and then to the rolling direction; the average FWHM is reported. In-plane mosaic is calculated from YSZ(111) and YBCO(113) ϕ scans. The contributions of the out-of-plane mosaic to the ϕ scan widths are removed, giving the true in-plane mosaic as would be measured by ϕ scans of a (100) reflection.[45]

Orientation mapping of YBCO grains was performed using electron backscatter diffraction (EBSD) in a field-emission SEM at a 70° sample tilt. Data for two-dimensional scans were taken on a hexagonal grid with a step size of 1 μm. Data filtering was performed to reduce incorrectly indexed points, but this filtering did not affect grain size or shape.

III. RESULTS

The J_c values for a set of RABiTS samples with YBCO film thicknesses out to 3 μm and a curve fit to these data are shown in Fig. 2. The data follow a one over square-root thickness dependence normalized by the average J_c of the 0.35-μm-thick films. This fit is represented by

$$J_c = A \cdot \mathrm{sqrt}(0.35/d) \quad , \tag{1}$$

where A is equal to 1.65 MA/cm^2 and d is the thickness of the YBCO film (in micrometers). Details of the fitting and relationships to starting template texture will be reported elsewhere.[41] Several of the data points are highlighted with references to microstructural features in some of the following figures. One data point from an IBAD YSZ sample is included in this figure and is denoted by the filled diamond. Also shown in Fig. 2 is a dashed line representing a minimum commercial performance level suggested by American Superconductor (Westborough, MA).[46] It is defined as a coated conductor having a current capacity of at least 300 A/cm width. The dashed line represents the J_c level that would be needed for a given thickness to obtain this level of performance.

Figure 3 contains SEM images of the general surface features and specific defect structures found in PVD BaF_2 YBCO films on RABiTS templates. These same features and defect structures were also found in IBAD YSZ samples. The general, submicron porous microstructure of the surface of the BaF_2-based films shown in Figs. 3(a) and 3(b) is from a 1.4-μm-thick, 1.7 MA/cm^2 YBCO film on a RABiTS template. This particular sample is shown in Fig. 2 to be substantially above the average J_c trend line. The porous surface structure is endemic to all of the BaF_2-based YBCO films. EDS analysis in the SEM and TEM showed the surface grains to be YBCO. The approximately 0.25-μm tabular or mesa-like YBCO surface grain structure was nearly identical from sample to sample, regardless of the thickness of the film or the template upon which it was deposited. For the high J_c sample of Figs. 3(a) and 3(b), this was the only structure observed on the surface of the sample.

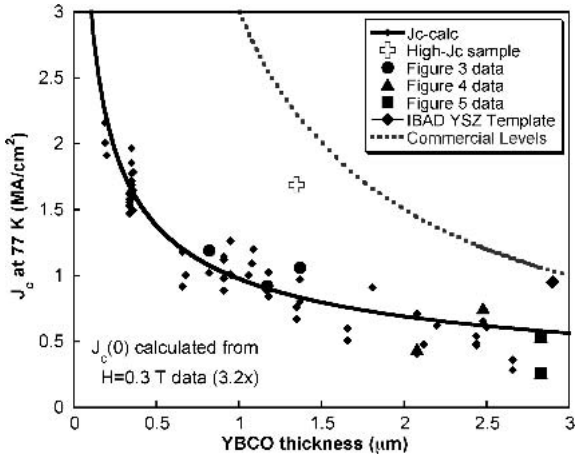

FIG. 2. Plot of J_c versus thickness for the RABiTS samples examined in this work. The J_c data are fit to a one over square root dependence on film thickness normalized to the average J_c of 0.35-μm-thick films. The dashed line represents the J_c values that are needed to obtain a commercially viable I_c performance level of 300 A/cm width.

Defects or deviations in the general surface structure were found for most of the other samples examined in this work. Variations in the apparent density of the surface structure are illustrated by a 1.4-μm, 1.05 MA/cm^2 YBCO RABiTS sample shown in Fig. 3(c). Likewise, Fig. 3(d) shows a 1.2-μm, 0.87 MA/cm^2 YBCO film on RABiTS with two different types of needle-shaped defects (A and B) that have intersected the film surface. One of the broadly shaped, type-A defects of the latter sample is illustrated in the micrograph of Fig. 3(e), which was from a 0.82-μm, 1.19 MA/cm^2 RABiTS sample. It can be described as a stack of plates that has been pushed over. A common feature of these broadly shaped defects was their association with one or more secondary phases (arrow) that were found by EDS to be Ba–Cu–O phases. Figure 3(f) shows a higher magnification image of the narrow, needle structures (type B) from the same 1.2-μm RABiTS sample of Fig. 3(d). The latter needles were identified as YBCO grains but as a rule were not *a*-axis-oriented grains. Misorientation of the *c* axis of the narrow-shaped YBCO grains relative to the film normal have been measured by EBSD to range from approximately 20° up to and including 90° (*a*-axis oriented). These structures will be shown in detail with cross-sectional TEM below. The three samples illustrated in Figs. 3(c)–3(f) are represented as solid circles in Fig. 2. They fall near the J_c averages for films of these thicknesses. This is consistent with the fact that most of the films that fell along or below the J_c curve fit had these surface defects.

The density of the surface defects can be correlated with J_c levels as demonstrated by the two 2.8-μm-thick YBCO films shown in Figs. 4(a) and 4(b). The J_c values at 77 K and self-field for each film were 0.52 and 0.26 MA/cm^2, respectively, and are shown in Fig. 2. Correlation with the XRD data of Table I shows that both of these films had nearly the same out-of-plane misalignment of 8° and 8.3° FWHM, respectively. However, the sample with the higher density of needle-shaped defects [Fig. 4(b)], had a very significant degradation of the in-plane alignment (almost 5°) based on true Φ measurements[45] of the YBCO and underlying YSZ in-plane misorientations.

The cross-sectional, SEM backscattered electron images in Figs. 5(a)–5(c) of three RABiTS samples of thickness 2.0, 2.5, and 5.0 μm show variations in the through thickness microstructure of these films. The corresponding J_c values at 77 K and self-field were 0.44,

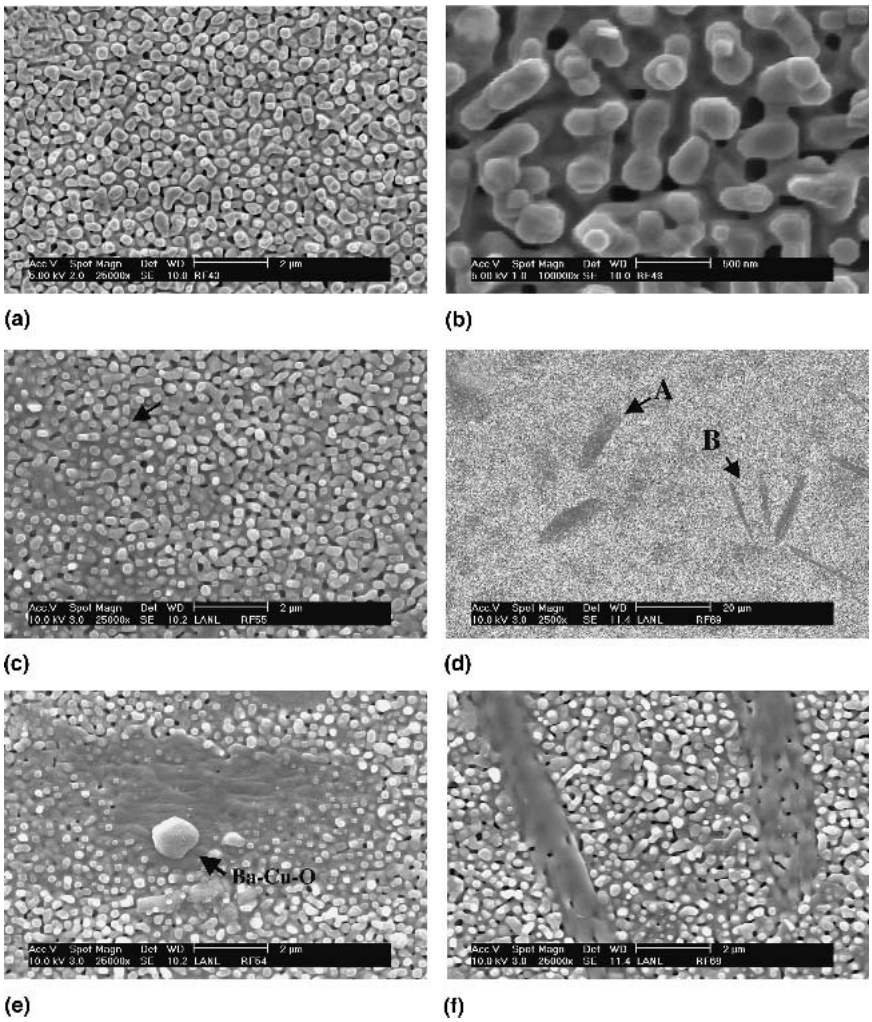

FIG. 3. SEM images of film surfaces from several RABiTS samples. Images (a) and (b) are from a 1.4-μm YBCO film that had a J_c of 1.7 MA/cm^2, a uniform surface morphology, and a J_c value that lies significantly above the fit line of Fig. 2. In other cases, deviations in the surface morphology arose from density variations or the formation of needle-shaped structures as indicated by the 1.4-μm and 1.2-μm YBCO films of (c) and (d), respectively. Higher magnification images of the two types of needle-shaped defects (A and B) shown in (d) are illustrated by the 0.82-μm and 1.2-μm YBCO films of (e) and (f), respectively. The broad needle shaped defects (type A) could often be found in combination with Ba–Cu–O secondary phases as indicated by the arrow in (e). All samples with surface defects had J_c values that lie close to or below the J_c fit line, as indicated in Fig. 2.

0.75, and 0.31 MA/cm^2, respectively. The first two samples are represented in Fig. 2 by the filled triangles. Figure 5(d) is a higher magnification image of Figure 5(c), which clearly shows the bimodal structure with an arrow indicating a second phase layer. Submicron precipitates within the YBCO grains are present in the lower half of the sample while the upper regions of the film contain larger secondary phases and some porosity. As a general rule, the division line for the bimodal structure was typically one half of the film thickness. However, deviations from this rule were found, as illustrated by the 2.5-μm-thick film of Fig. 5(b). The bottom region of the bimodal structure was approximately one fourth of the film thickness and the corresponding J_c value was nearly twice as high as for the 2.0-μm-thick film shown in Fig. 5(a).

Specific details of the bimodal structure can be found in the TEM, STEM, and spectral images of Figs. 6 and 7. Figures 6(a) and 6(b) are TEM images of the 2.5-μm YBCO film on RABiTS [Fig. 5(b)] and a 2.9-μm YBCO film on IBAD YSZ, respectively. Figure 7 contains STEM, TEM, and spectral images that show in greater detail the bimodal microstructure of the 2.5-μm-thick YBCO film on RABiTS. The bimodal structure consists of two very distinct regions. The bottom layer of the structure is composed of large, well-formed YBCO grains with many Y_2O_3 precipitates and only a few planar defects while the upper region consists of small YBCO grains containing a few precipitates, a higher number of planar defects, and discrete secondary phases such as Y_2O_3, $Y_2Cu_2O_5$, $Ba_2Cu_3O_y$, $BaCu_2O_y$, and/or Ba–O–F. The structure and distribution of phases are

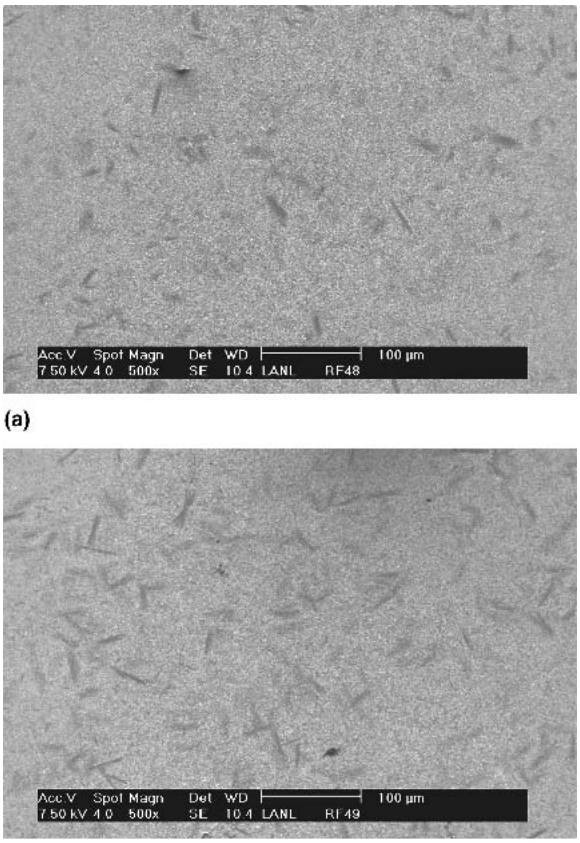

FIG. 4. SEM images of two 2.8-μm YBCO films on RABiTS templates that had different densities of surface defects. The film shown in (a) had a J_c of 0.52 MA/cm^2 while the one in (b) had a J_c of 0.26 MA/cm^2.

shown in the elemental STEM maps of Fig. 7. The Y_2O_3 particles are layered within the large YBCO grains at the bottom of the spectral images. A layer of an unidentified Ba–O–F phase separates the two regions of the bimodal structure. Discrete secondary phases of $Y_2Cu_2O_5$, Ba–Cu–O, and/or Ba–O–F are found in the top region of the bimodal structure. The Ba–O–F phase was often found in combination with CuO. Note that the sample referred to in Figs. 6(a) and 7 had a somewhat atypical bimodal structure for this study in that the large grain material comprised only about ¼ of the film thickness. Additional layers of large-grain YBCO and $Ba_2Cu_3O_y$ or Ba–O–F with CuO were often found when the thickness of the bottom region comprised about ½ of the film thickness. However, the overall microstructure of samples with multiple layers of YBCO and $Ba_2Cu_3O_y$ or Ba–O–F in the bottom half of the film are still considered to be bimodal based on YBCO grain size in the two regions of the film.

Figure 7 shows a Ba–O–F phase as the main Ba-containing secondary phase. In other samples, $Ba_2Cu_3O_y$ is found instead of Ba–O–F/CuO. The presence of either Ba-containing secondary phase appears to depend upon the thickness of the film, the overgrowth by YBCO grains, and the amount of time spent at the high temperatures of the conversion process. With respect to the thicker films, it is thought that overgrowth of the Ba–O–F/CuO layers by the large YBCO grains in the lower half of the films may isolate the layers and inhibit or prevent water from reaching them to complete the reaction to form $Ba_2Cu_3O_y$. Even smaller, discrete Ba–O–F phases in the top regions of the film may become metastable if YBCO grains overgrow and encapsulate the F-containing secondary phases.

Figure 8 is an EBSD map of the large grain YBCO structure near the bottom of a 2.9-μm YBCO film grown on an IBAD YSZ template. The top half of the bimodal structure of the sample was removed by ion milling. Several of the grains in the plane of the film are in excess of 50 μm. With respect to the YBCO film, the lateral dimensions of these grains are more than 17 times the film thickness. The TEM, STEM, and EBSD data of Figs. 6, 7, and 8 provide strong evidence for enhanced liquid-phase assisted growth of the large YBCO grains in the bottom region of the bimodal structure. Note that the average grain size of the IBAD YSZ/CeO_2 template on which epitaxial growth of YBCO is supposed to occur is only in the range of 0.1–0.25 μm.

Figure 9(a) is a set of microdiffraction patterns taken from a stack of layers in a 2.9-μm-thick YBCO IBAD YSZ sample as shown in the TEM bright-field image of Fig. 9(b). This is an example of the multiple layers of large-grain YBCO and a Ba-containing second phase commonly found in the bottom half of the bimodal structure. The selected-area diffraction pattern of Fig. 9(c) shows the [010] zone axis of the bottom YBCO grain properly aligned with the [110] zone axis of the underlying IBAD YSZ template. A lower magnification image of the overall structure is shown in the TEM bright-field image of Fig. 9(d). After the full processing cycle, the CeO_2 layer that separates the IBAD YSZ from the YBCO has completely reacted to form a $BaCeO_3$ layer that is not aligned to either the YBCO or IBAD YSZ. This reaction to form an unaligned $BaCeO_3$ layer was also observed for the RABiTS samples examined in this work and in previous work on pulsed laser deposited YBCO films on CeO_2-buffered IBAD YSZ templates.[47] Above each layer of $Ba_2Cu_3O_y$, the YBCO grains are observed to have a significant out-of-plane tilt. The tilt increases from 3.0° to 6.5° with the addition of a second $Ba_2Cu_3O_y$ layer. The presence of these $Ba_2Cu_3O_y$ second-phase layers correlates with increases in the mosaic spread of the out-of-plane and in-plane alignment as measured by XRD. A comparison of XRD measurements on YBCO films of nominally the same thickness with or without the presence of second phase layers can be found in Table I.

Correlations with the surface defects observed by

Table I. XRD and J_c data for selected RABiTS samples from this study. $\Delta\phi$ are true in-plane mosaic. The presence of second phase (SP) layers such as $Ba_2Cu_3O_y$ or Ba-O-F/CuO as determined by TEM are indicated.

		In-plane mosaic (FWHM)			Out-of-plane mosaic (FWHM)				
tYBCO (μm)	J_c (MA/cm^2)	$\Delta\phi_{YBCO}$ (degree)	$\Delta\phi_{YSZ}$ (degree)	$\Delta\phi_{YBCO}-\Delta\phi_{YSZ}$ (degree)	$\Delta\omega_{YBCO}$ (degree)	$\Delta\omega_{YSZ}$ (degree)	$\Delta\omega_{YBCO}-\omega_{YSZ}$ (degree)	Porosity	SP Layers
1.4	1.05	5.9	5.8	0.1	5.8	5.2	0.6	No	Yes
1.4	1.69	5.8	5.7	0.1	6.1	6.6	–0.5	Yes	No
1.8	0.9	6.0	5.8	0.2	5.9	5.4	0.6	Yes	No
2.0	0.4	8.2	6.2	2.0	6.8	5.7	1.1	No	Yes
2.8	0.52	7.7	7.1	0.6	8.3	5.5	2.8	⋯	⋯
2.8	0.26	10.8	6.0	4.8	8.0	5.2	2.8	⋯	⋯

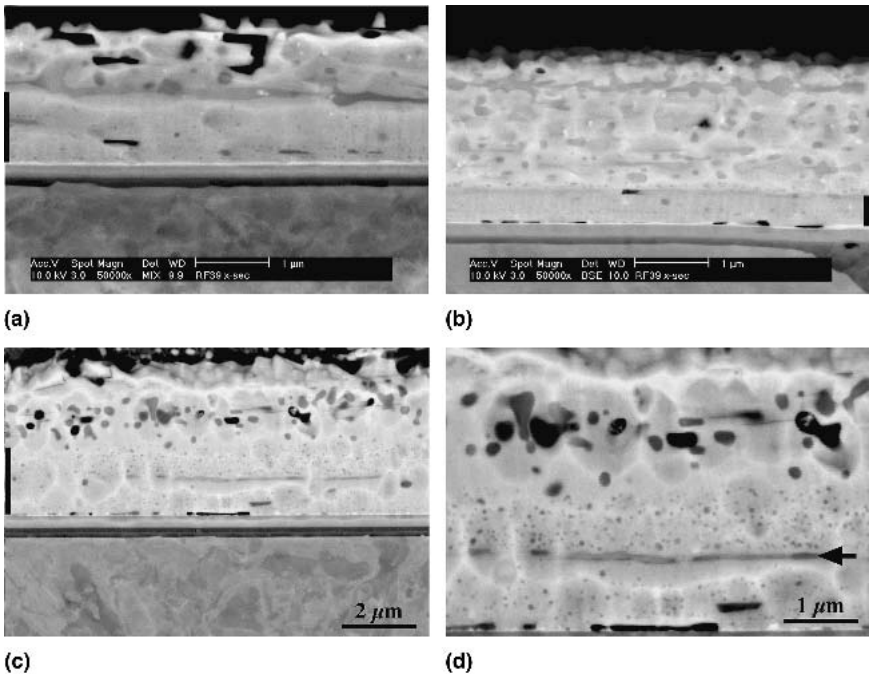

FIG. 5. SEM cross-sectional images of three RABiTS samples with YBCO films of thickness (a) 2 μm, (b) 2.5 μm, and (c, d) 5.0 μm. A bimodal structure within the YBCO films is evident in the cross sections. The heavy black lines designate the bottom region of the bimodal structure. The J_c values of the films were 0.4, 0.75, and 0.35 MA/cm^2, respectively. A higher magnification of the bimodal structure of the 5.0-μm-thick film is shown in (d). A second phase layer is indicated by the arrow.

SEM can be made with the cross-sectional TEM data. Figures 10(a) and 10(b) show examples of the two different types of needle-shaped defects (types A and B) found in these samples and illustrated in Fig. 3. The type-A structure of Fig. 10(a) is believed to be indicative of low angle misalignments of YBCO colonies. In cross-sectional TEM, these low-angle, misaligned colonies are tilted, relative to the film normal by just a few degrees. Layers or discrete grains of $Ba_2Cu_3O_y$ or Ba–O–F can be found along the lower boundary of the tilted colony. The type-B defects of Fig. 10(b) appear to be *a*-axis-oriented YBCO. However, TEM diffraction and EBSD analysis have shown these needles to have *c*-axis misorientations ranging from 20° to 90° relative to the film normal. In the example shown in Fig. 10(d), the *c*-axis of the needle phase is oriented 72° from the film normal. It appears to have nucleated at the interface in a region of the film where there was a defect in the CeO_2 layer. In this localized region or pinhole defect, the CeO_2 layer is much thinner than intended and in places, missing altogether. The reaction layer beneath this misoriented YBCO grain consisted of both $BaCeO_3$ and $BaZrO_3$. The latter phase comes from reaction with the YSZ layer exposed due to missing or depleted CeO_2.

The second phase layers form during the precipitation of the large YBCO grains during the conversion process. Shown in Fig. 11 is a 2.7-μm-thick precursor film on a RABiTS template quenched from a temperature of 780 °C after 1.5 h into the conversion process (0.5 h into the "growth" step). Figures 11(a) and 11(b) are TEM and STEM images of the full cross section of the sample. Figure 11(c) contains elemental maps of the area outlined in the STEM image. The Ba, Cu, and Y maps show the elemental distributions of the cations. The F map is a

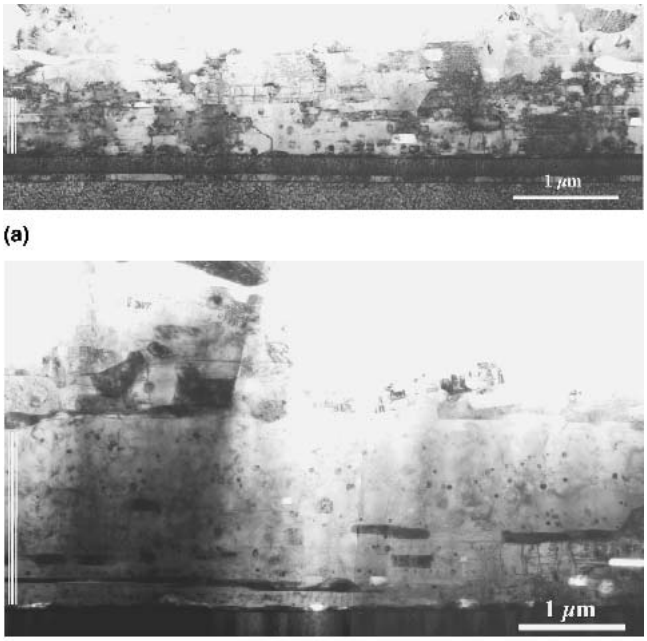

FIG. 6. Cross-sectional TEM images of fully developed bimodal structures in (a) a 2.5-μm-thick YBCO film on a RABiTS template and (b) a 2.9-μm-thick YBCO film on an IBAD YSZ template. The bottom part of the structure, denoted by the white bar on the left side of the micrographs, consists of large YBCO grains with Y_2O_3 precipitates. The top region consists of smaller YBCO grains with a high density of planar defects, fewer precipitates, and many more discrete secondary phases.

little more ambiguous as it seems to suggest that F can be found everywhere in the composite. This can be explained by limitations in EDS in eliminating peak overlap from the low-energy peaks (OK, CuL, etc.) surrounding the F peak. To qualify the presence of F by EDS, individual spectra from the data set were examined to determine whether F was present at a particular point in the map. From this process, it was found that F is clearly present with the Ba in the precursor and in the second phase layers between the YBCO grains in the bottom of the film. It is not believed to be present to a degree detectable by EDS in the $Y_2Cu_2O_5$, CuO, or YBCO phases in the film or in the underlying buffer layers. Segregation of CuO in the early stages of the process is indicated by the Cu map of Fig. 11(c). The CuO segregation was also seen in SEM images of the film surface. The rest of the precursor film, prior to conversion, is composed of $Y_2Cu_2O_5$ and Ba–O–F. The $Y_2Cu_2O_5$ is present as a well-defined phase while the Ba–O–F appears to form a continuous matrix surrounding the $Y_2Cu_2O_5$.

In this quenched sample, several large YBCO grains have already precipitated from the precursor along the interface with the underlying buffer layers. The relative extent of the conversion is indicated by the width of the white bars on the left side of Fig. 11(a). The layered structure of YBCO and Ba–O–F/CuO reveals a laminar growth process that is characteristic of the ex situ conversion of BaF_2-based YBCO films. Within these large YBCO grains are layers of Y_2O_3 precipitates. At the growth front of the YBCO grains, Y_2O_3 particles are present within the Ba-O-F phase as indicated by the arrows in the Y elemental map. Based on the two main precursors, an overall conversion process for the bottom half of the bi-modal structure can be written as

$$(3)\ Y_2Cu_2O_5 + (4)\ \text{Ba-O-F} + (x)\ H_2O \Rightarrow (2)\ YBa_2Cu_3Oy + (2)\ Y_2O_3 + (y)\ HF \quad . \quad (2)$$

The amounts of H_2O and HF depend on the composition and structure of the Ba–O–F phase, which has not yet been determined. The excess Y_2O_3 appears to precipitate ahead of the growth front and is then incorporated as the YBCO grains overgrow them. The formation of these large YBCO grains in the bottom half of the bimodal structure suggests a liquid-mediated growth process. The exact composition of the liquid phase from which the YBCO precipitates has not yet been determined. Most likely, one or more intermediate reactions occur between the $Y_2Cu_2O_5$ and Ba–O–F in the presence of water, and Eq. (2) is a somewhat simplified view of the conversion process.

During the conversion process, the CuO that migrates to the top of the film during the initial stages of conversion is consumed during the remainder of the process to form YBCO and other secondary phases; CuO is not observed, to any large extent, in the final phase assemblage of the films. The reaction dictating the conversion of the YBCO from the precursors in the top region of the films will be somewhat different from Eq. (2) due to the excess copper oxide. The secondary phases found in fully converted YBCO films were $Y_2Cu_2O_5$, Y_2O_3, $BaCu_2O_y$, and $Ba_2Cu_3O_y$. In some cases, the combination of Ba–O–F/CuO was found in place of the barium cuprates. The YBCO found in the upper region of the films is heavily faulted with the lattice spacing of the intergrowths corresponding to the copper-rich $YBa_2Cu_4O_y$ (Y-124) and $Y_2Ba_4Cu_7O_y$ (Y-247) phases. Likewise, the additional secondary phase, $Y_2Cu_2O_5$, reflects the different overall chemistry and/or the slightly different reaction path of the upper region of the film. In the bimodal structure, $Y_2Cu_2O_5$ is not a precipitate in the large YBCO grains of the bottom region.

Figures 12(a) and 12(b) show the Y_2O_3 particles within the large YBCO grains at the film bottom imaged under diffraction conditions of $g = \langle 100 \rangle$ and $g = \langle 001 \rangle$, respectively. The vertical, banded structure seen in Fig. 12(a) is the twin spacing within the grain. It is clear that some defect structures are larger than the physical size of the precipitate. In the *ab* plane, several finite planar defects extend away from the Y_2O_3 particles. Very little

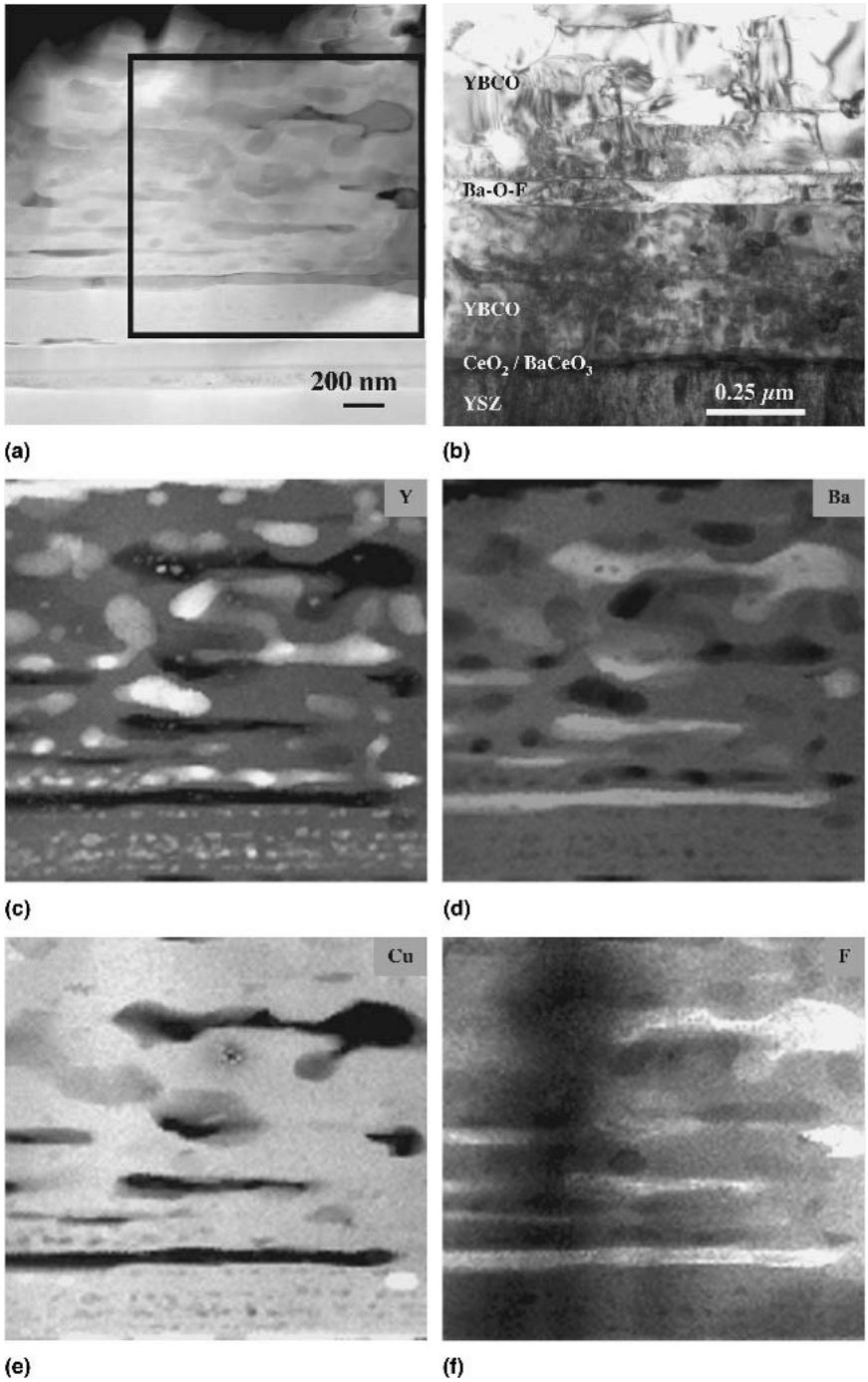

FIG. 7. (a) STEM dark-field and (b) TEM bright-field images of a 2.5-μm-thick film on a RABiTS template. Spectral images corresponding to the box outlined in (a) are shown in (c–f). The Y, Ba, and Cu maps [(c–e), respectively] show the cation distribution through the thickness of the film. (f) The F map shows that F is present with the phase containing only Ba and O (O map not shown). Examination of the individual EDS spectra from other spots in the map show that F is not present in the YBCO grains or in the other secondary phases. The residual contrast in the F map results from difficulties in separating it from other nearby peaks in the low energy range of the EDS spectrums used to construct the map.

strain contrast is observed around the spherical particles when g is of a $\langle 100 \rangle$ type reflection. This indicates a relaxation of the YBCO matrix that is coplanar with the Y_2O_3 through the formation of the finite planar defects. Conversely, the micrograph of Fig. 12(b) shows strain contrast in the surrounding YBCO film oriented along the c axis or film normal. TEM does not show any planar defects within the YBCO either above or below the spherical particles. Hence, the precipitates within the large YBCO grains are part of a defect structure that is also composed of planar defects and strain within the adjacent YBCO.

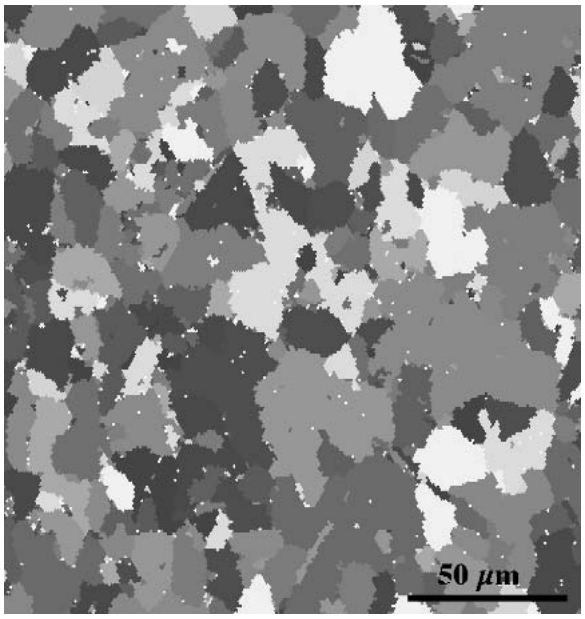

FIG. 8. EBSD map showing the large YBCO grain structure in the bottom region of the bimodal structure of a 2.9-μm YBCO IBAD YSZ sample. The YBCO structure in the bottom region was imaged by EBSD after the top region of the film was milled away. Some grain sizes exceed 50 μm, which is more than 17 times the YBCO film thickness. The underlying grain size of the IBAD YSZ layer is on the order 0.1–0.25 μm based on TEM observations in cross-section.

The structures above grain boundaries in the NiW (3 at.%) substrate can become complex with the presence of extended second-phase structures coupled with the laminar growth mode of the YBCO film. Shown in Fig. 13 is a TEM composite micrograph of a 1.4-μm YBCO film above such a grain boundary in a RABiTS sample. The local structure of the YBCO film follows the underlying alignment of the buffer layers and NiW substrate. The short-dash line shows the meandering boundary determined by the change in alignment of the YBCO as one traverses the grain boundary in the substrate. In addition, the long-dashed white lines indicate second phases of $Ba_2Cu_3O_y$. One of these short second-phase layers covers part of the grain boundary. The combination of the meandering grain boundary and second-phase layers illustrates the lateral growth mode of the YBCO film in the presence of a liquid phase. The effects on connectivity between YBCO regions delineated by Ni grain-boundary structures propagating into the films are unknown at this point.

Cross-sectional TEM of films having no surface defects, such as the 1.4-μm YBCO film shown in Figs. 3(a) and 3(b), revealed some interesting differences in the microstructures that are important to understand in terms of optimizing the performance of these thick PVD-BaF_2 films. Shown in Figs. 14(a), 14(b), and 14(c) are, respectively, cross-sectional STEM dark-field, TEM bright field, and EDS spectral maps of the 1.4-μm-thick film of Figs. 3(a) and 3(b) that had a J_c of 1.7 MA/cm^2. Figures 15(a) and 15(b) are composite micrographs of the same 1.4-μm YBCO film and an additional 1.8-μm YBCO RABiTS sample that was also free of surface defects. The STEM and TEM images of Figs. 14(a) and 14(b) suggest a through-thickness uniform microstructure in this particular area of the sample. The spectral maps of Fig. 14(c) do not show second-phase layers, and they show the presence of $Y_2Cu_2O_5$ throughout the film. In other words, this region of the 1.4-μm-thick film did not contain a bimodal structure. The arrows at the top of the Y and Cu maps point out the differences between the Y_2O_3 and $Y_2Cu_2O_5$ phases. The Cu maps do not show change in contrast between the $Y_2Cu_2O_5$ and YBCO phases. The arrows at the bottom of the Y and Cu maps point out the presence of $Y_2Cu_2O_5$ secondary phases. Within the large grains of YBCO in the bimodal structures shown previously, only Y_2O_3 would have been expected to be present. However, the TEM micrograph of Fig. 15(a), which is from a different area of the 1.4-μm YBCO RABiTS sample, suggests that vestiges of the bimodal structure are still present in the film. Figure 15(a) shows an area of the 1.4-μm film where large-grain YBCO material containing Y_2O_3 precipitates occupies approximately half of the film thickness, yet contains no second phase layers. Some porosity lies along part of the line that divides the bimodal structure, as indicated in Fig. 15(a). The porosity may indicate that second-phase layers formed during the initial stages of the conversion process were able to diffuse away and react to form more YBCO elsewhere. A different 1.4-μm YBCO RABiTS sample with second-phase layers and less internal porosity is shown in Fig. 13. The XRD data for these two 1.4-μm-thick YBCO films on RABiTS can be found in Table I. There is no apparent change in the in-plane texture for either sample, relative to the underlying YSZ buffer layer. However, the out-of-plane mosaic increased for the sample with the second phase layers, while it decreased for the sample without the second-phase layers.

Figure 15(b) contains a composite TEM micrograph of a 1.8-μm-thick YBCO RABiTS sample. This composite was also devoid of surface defects, although the J_c was only slightly better than average as indicated in Fig. 2. TEM analysis again showed very few second phase layers in the 1.8-μm-thick film. A close examination of the TEM image of Fig. 15(b) shows a uniform, through-thickness microstructure on the left side. Both Y_2O_3 and $Y_2Cu_2O_5$ particles were uniformly distributed throughout the film. On the right side, a large YBCO grain with only Y_2O_3 precipitates was found that defines the bottom region of a bimodal structure. The arrow indicates the point at which the large grain ends within the film. There was no second-phase layer separating the large YBCO grain from the rest of the film. Comparison of the XRD data of

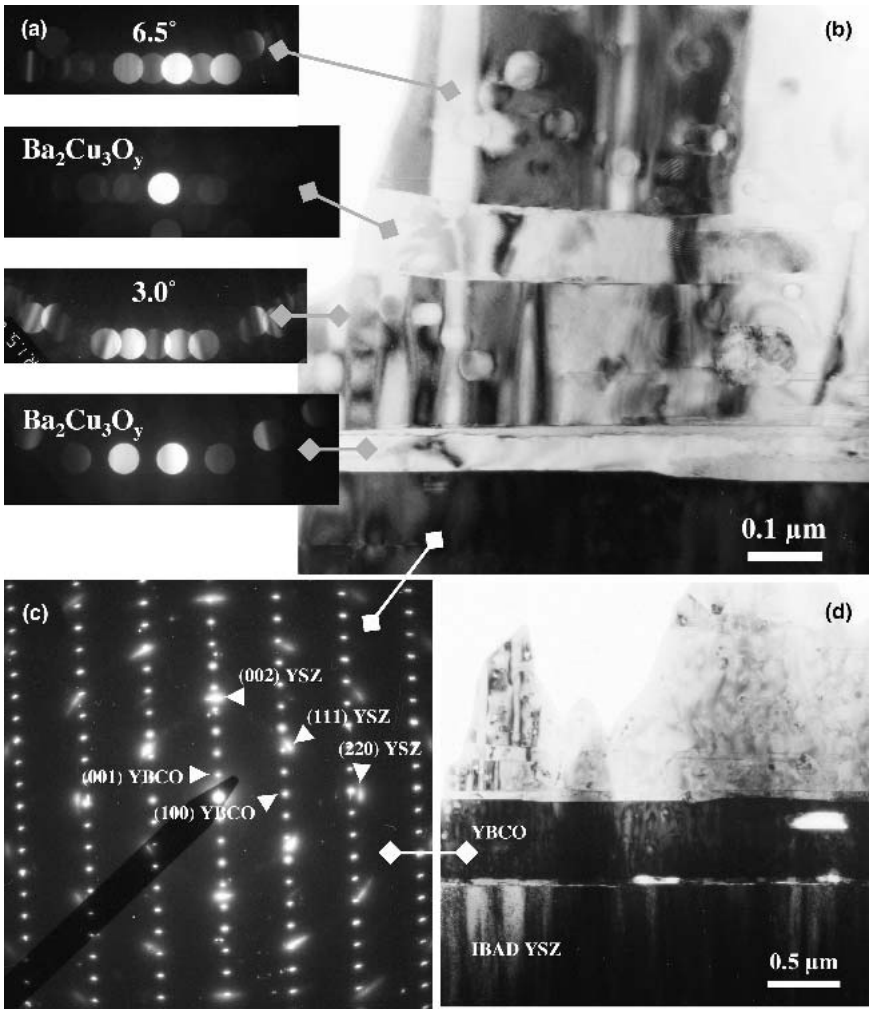

FIG. 9. (a) TEM microdiffraction and (b) bright-field image showing the progression of out-of-plane tilt in several YBCO grains with intervening $Ba_2Cu_3O_y$ layers. The bottom YBCO grain is oriented so the beam is parallel to [010] zone axis as indicated by the selected area diffraction micrograph in (c). A larger view of the structure is shown by the TEM bright-field image in (d).

this 1.8-μm film with a 2.0-μm film [Fig. 5(a)] shown previously reveals that the latter sample with the second phase layers had a significant increase in the in-plane mosaic spread, relative to the underlying YSZ buffer layer. It also had a larger increase in the out-of-plane alignment compared to the 1.8-μm-thick film that did not have the second phase layers.

IV. DISCUSSION

The BaF_2-based, YBCO films are characterized by laminar film morphologies due to the lateral growth, relative to the interface, of the superconducting phase from a transient liquid during the ex situ conversion. The conversion process starts at the buffer layer/precursor interface and proceeds toward the film surface. Manifestations of this growth mode are multiple grains through the thickness of the film, large grain growth, and grain boundary meandering. YBCO grain sizes in excess of 50 μm were observed by TEM and EBSD in the bottom region of the bimodal structure of the PVD-BaF_2 films. These grain sizes are greater than 17 times the starting film thickness. Only grain growth from a liquid phase could account for the large grain sizes in a system where the growth is confined by the two-dimensional nature of the film. In contrast, a columnar structure is obtained from the in situ PVD process of pulsed laser deposition (PLD) of YBCO films on comparable textured templates.[47] In the latter case, one grain more or less spans the thickness of the film. The columnar size in PLD YBCO films is typically 0.25–0.5 μm.

The bimodal structure describes two different regions of YBCO that form due to slightly different reaction routes. Copper oxide segregation to the top of the film during the early stages of the conversion process results in a Cu-deficient bottom region. A defining characteristic of the bottom portion of the bimodal structure is the large, well-formed YBCO grains containing spherical

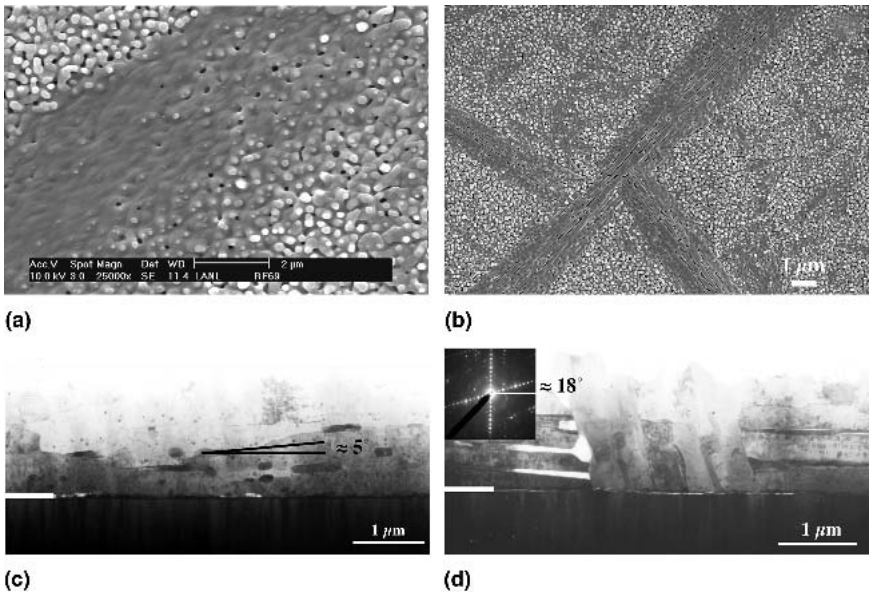

FIG. 10. SEM images of the surface morphology from (a) 1.2-μm YBCO film on a RABiTS template showing the broad needle-shaped (type A) defects and (b) 2.0-μm YBCO film on an IBAD YSZ template illustrating the narrow, needle-shaped (type B) defects. The cross-sectional TEM bright-field images in (c) and (d) show the correlations between the internal microstructures (arrows) and the two types of surface defects shown in (a) and (b), respectively. The type-A defect appears to be a YBCO colony with a small tilt, which in the example (c) is tilted at 5° relative to the film normal. The type-B defect in (d) is a narrow YBCO colony whose *c* axis is tilted 72° from the film normal.

precipitates of Y_2O_3. These precipitates are part of an extended defect structure that includes the finite intergrowths or planar defects localized in the *ab* plane around the precipitates and the anisotropic strain in the YBCO matrix above and below the Y_2O_3 particles. These defects are probably beneficial as correlated defects in both the *ab* plane and along the *c* axis of the YBCO are desirable for improving the flux pinning in these coated conductors. The Y_2O_3 particles separate out ahead of the growth front as part of the reaction denoted by Eq. (2). They are subsequently overgrown by the YBCO grains, and the distance between the Y_2O_3 layers indicated in the spectral maps gives a measure of the thickness of a growing YBCO lamella.

One or more second-phase layers of $Ba_2Cu_3O_y$ or Ba–O–F/CuO could often be found along the basal plane of large YBCO grains. The presence of either one apparently depends on the annealing time, not the overall composition. Samples held for longer times at 780 °C were more likely to contain $Ba_2Cu_3O_y$ rather than the Ba–O–F phase. However, the point at which this changeover occurs is still not well understood. $Ba_2Cu_3O_y$ is not found in most of the published phase diagrams and never at the end of a direct tieline with Y_2O_3.[48] Phase fields involving Y_2BaCuO_5 (Y-211) separate Y_2O_3 from the barium cuprates. That no Y-211 is found in these films may reflect the instability of this phase in films, as reported recently.[49] As suggested by Jo et al., different phase equilibria may exist in YBCO films processed under conditions very different from those of bulk samples.[50] The formation path and structure of the film may also play a role in determining a metastable phase assemblage. The enclosure of the Y_2O_3 particles within the YBCO grains forms a stable structure. Further reactions between the second-phase layers and Y_2O_3 particles to form YBCO are inhibited. Likewise, the possibility exists for overgrowth and encapsulation of the Ba–O–F/CuO layers by the large YBCO grains. These layers may then be isolated from the water source, and a conversion to $Ba_2Cu_3O_y$ and/or more YBCO is hindered or blocked.

The top region of the bimodal structure consists of smaller YBCO grains with higher densities of planar defects, fewer internal precipitates, porosity, and discrete secondary phases such as $Y_2Cu_2O_5$, Y_2O_3, or several Ba–Cu–O phases. The dividing line between the two regions tended to lie at half the film thickness, though exceptions to this rule could be found as noted above. The YBCO in the top region of the film is also thought to form with the assistance of a liquid phase, although the reaction governing the formation is thought to be slightly different from Eq. (2) due to the extra CuO that segregated to this region, as indicated in Fig. 11. It is believed that there is less liquid phase in the top half of the film during the conversion of the precursor relative to the amount present in the bottom region when it converted. The larger grains in the bottom are thought to come from a "bulk-like" solidification process involving a substantial volume of liquid. On the other hand, the smaller YBCO grains in the top half are thought solidify from a thin interfacial liquid layer separating the precursor and

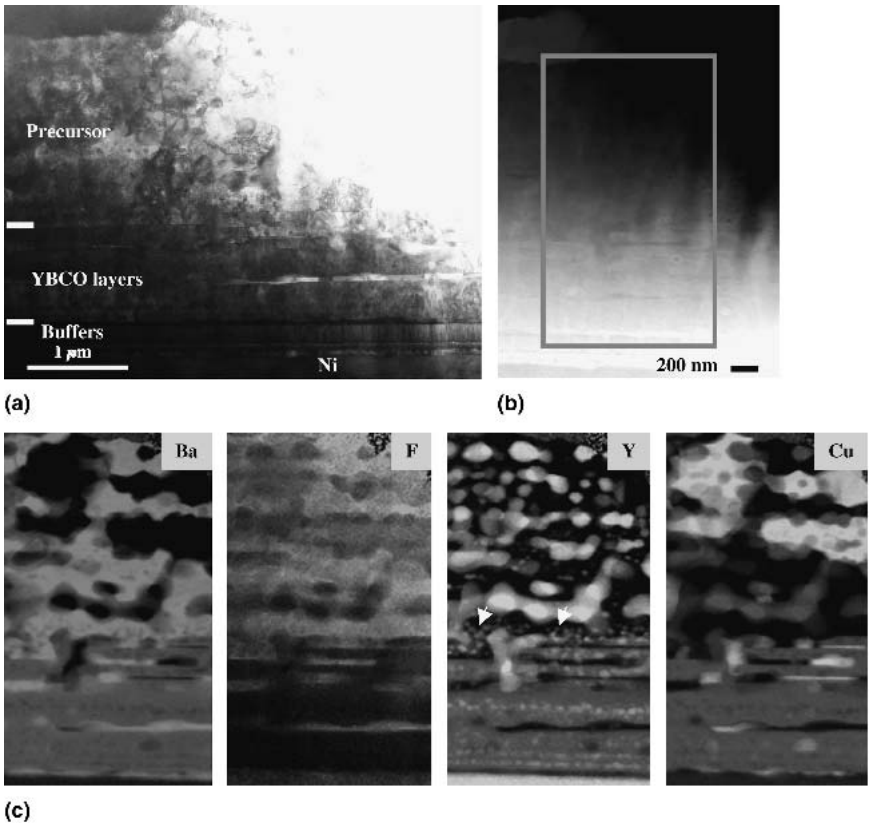

FIG. 11. (a) TEM bright-field and (b) STEM dark-field images of a 2.9-μm RABiTS sample after a partial heat treatment at 780 °C and dry-ambient quench. The box in (b) indicates the scanned region used to form the Ba, F, Y and Cu spectral images in (c). The two white bars at the left of the image (a) indicate the extent of the YBCO conversion process. The lower bar is at the interface with the underlying buffer layers. A discussion of all the phases can be found in the text.

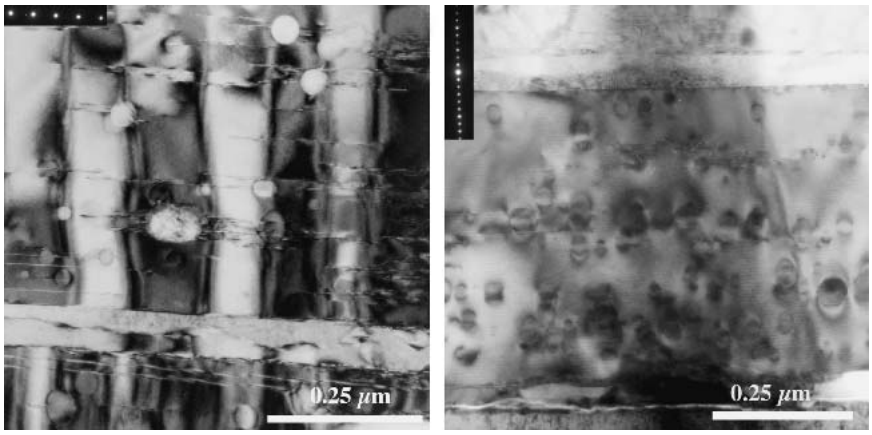

FIG. 12. TEM images of the Y_2O_3 precipitates in the large YBCO grains of a 2.9-μm YBCO film on an IBAD YSZ template imaged with diffraction conditions (a) $g = \langle 100 \rangle$ or (b) $g = \langle 001 \rangle$. Note the anisotropic strain contrast along the *c* axis. The short stacking fault structures in the *ab* plane appear to have relieved the strain in the surrounding YBCO that is co-planar with the precipitate. The banded contrast seen in (a) arises from the twin structure of the large YBCO grain.

YBCO. The latter process is what one would like to occur throughout the film to achieve a uniform, through-thickness microstructure.

Other works on BaF_2-based YBCO films have reported or inferred the presence of liquid phases in the growth of the YBCO. Large YBCO grains with Y_2O_3 precipitates, CuO segregation, and thin layers of an apparent liquid phase were observed by Wu et al. in previous work with PVD BaF_2-based YBCO films.[35] One difference was that a Y–Ba oxyfluoride was reported in the latter work while the present work showed segregation into $Y_2Cu_2O_5$ and Ba–O–F prior to conversion into

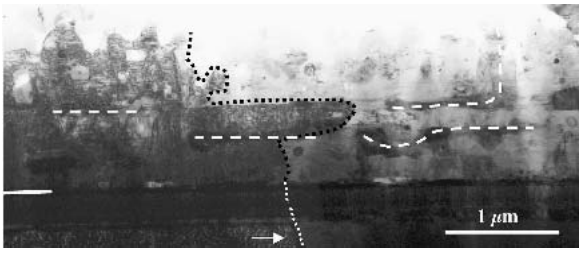

FIG. 13. TEM image of a meandering grain boundary (short dash line) within the YBCO film and above a grain boundary in the Ni substrate of a RABiTS sample. The presence of the Ba–Cu–O layers (white long-dashed lines) and meandering grain boundary clearly illustrates the effects of the laminar growth mode of these films. The solid white line at left denotes the boundary between the YBCO and underlying buffer layers.

YBCO. These different phase assemblages may be due to differences in the processing conditions. They also suggest the possibility of several different reaction routes to form YBCO in the ex situ process. The role of liquid phases in the conversion process was also inferred by McIntyre et al. and Yoshizumi et al. in work with MOD BaF_2 YBCO films.[18,51] Yoshizumi et al. noted the initial decomposition of the BaF_2 without the immediate formation of YBCO based on measurements of the F content. The authors postulated a conversion into BaO. Based on the TEM in the present work, the expectation was that the reduction in the amount of F would be consistent with observed formation of a Ba–O–F phase. Thicker films were also found to have a higher F/Ba ratio, and it was postulated that the processing of thicker films would lead to enhanced melt formation. This hypothesis is consistent with our observed results of the bimodal structure roughly dividing the film in half and the presence of the very large YBCO grains in the thick films.

The exact composition of the liquid phase is not known at this time and will be the subject of future work.

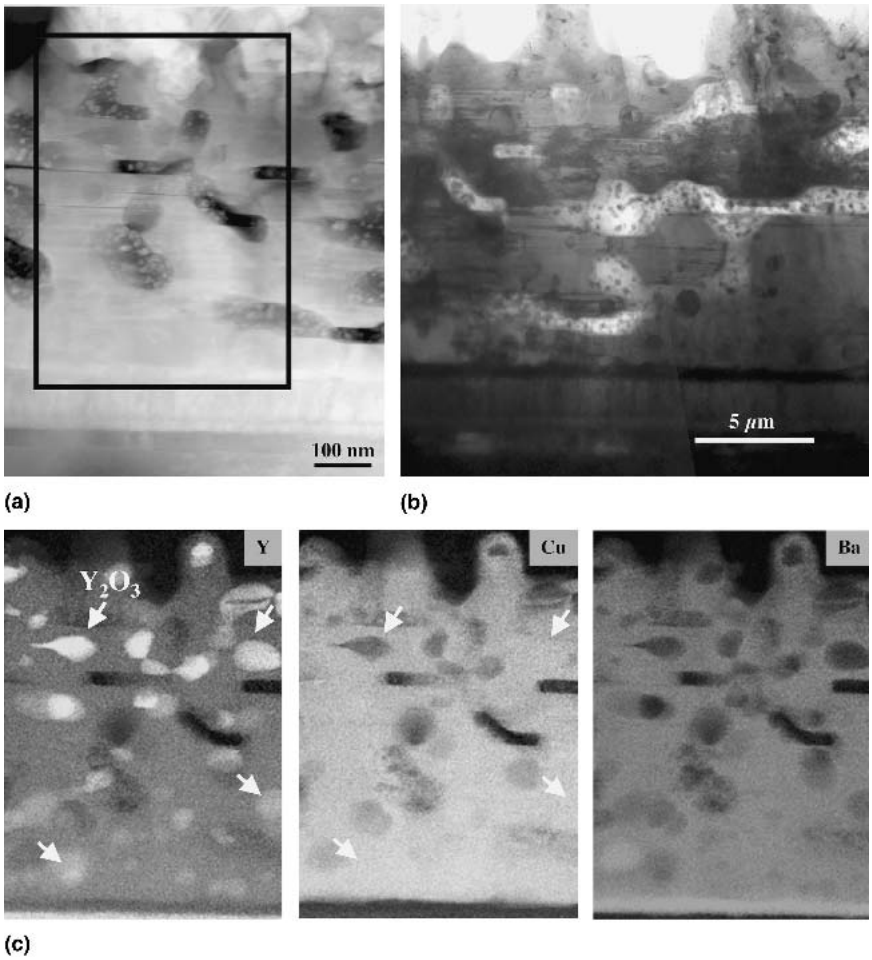

FIG. 14. (a) STEM dark-field, (b) TEM bright-field, and (c) EDS spectral maps showing the absence of second phase layers in a 1.4-μm high-J_c YBCO film from a RABiTS sample. This sample is indicated in Fig. 2 to lie substantially above the average J_c fit line. The relatively uniform distribution of secondary phases in the sample suggests the absence of a bimodal structure in this region of the sample. The arrows in the top regions of the Y and Cu maps denote the differences in contrast between the Y_2O_3 and $Y_2Cu_2O_5$ secondary phases. The arrows in the bottom halves of these two spectral images also show the presence of $Y_2Cu_2O_5$. In the bimodal structure described in the text, only Y_2O_3 precipitates would be expected in the bottom region.

Wong-Ng et al. have published data regarding the formation of low melting liquids within the Y,Ba,Cu//F,O system.[52] They found, in the presence of water, no stable liquid phase formation below 815 °C at 0.02% $P(O_2)$ within the $BaO–Y_2O_3–CuO–BaF_2$ system. However, they could not rule out the formation of transient phases. Only when they considered more F-rich compositions did they encounter stable liquid phases below 600 °C. The starting compositions of the films used in this work do not fall into the latter regions of the phase diagram. Thus liquid phase formation during film conversion is believed to be a transient event, and Eq. (2) presents a simplified view of the conversion process. The liquid phase composition and details of the conversion process are the topic of current research and will be published at a later date.

Comparisons of the data in Table I for films of nominal thickness 1.4 and 2.0 μm show a correlation between the presence of either $Ba_2Cu_3O_y$ or Ba–O–F/CuO second-phase layers, lower J_c levels, and larger mosaic spreads for the in-plane and out-of-plane alignment of the YBCO films. The detrimental effects of the second phase layers are clearly seen in Fig. 9, where each subsequent $Ba_2Cu_3O_y$ layer increased the out-of-plane alignment of the YBCO grain directly above them. The presence of the layers appears to be a result of YBCO grains overgrowing and isolating Ba–O–F/CuO layers, as shown in Fig. 11. Note that the presence of the second-phase layers also correlates closely with the presence of surface defects, as shown in Figs. 3 and 10. Hence, SEM examination of the film surface can be used to give a quick indication of the types of defect structures that may be present within the film. The 1.4-μm-thick film with J_c substantially higher than the average for the series of RABiTS samples examined in this work had neither surface defects nor second phase layers. One other 1.8-μm RABiTS sample that was found to have no surface defects and no second phase layers had a J_c that was slightly above average. In both cases, vestiges of the bimodal structure remained although the bimodal structure varied from point-to-point and in some places was absent. In both cases, a smaller mosaic spread in $\Delta\Phi$ and $\Delta\Omega$ was found in the absence of the second phase layers. In the case of the 1.4-μm-thick film, a substantially higher J_c level was obtained. A reduction in the thickness of the lower region of the bimodal structure was also found to correlate with higher J_c values, as indicated in Fig. 5. A thinner bottom layer is thought to result in fewer second phase layers. As shown in Fig. 9, the degradation in out-of-plane misalignment increased with each additional second phase layer.

In spite of the detrimental aspects that the excessive amounts of the liquid phase can cause, we believe that the most efficient conversion of the precursor into an epitaxially aligned YBCO film occurs via an intermediate liquid phase. This appears to hold true regardless of whether one is using the PVD-BaF_2 or MOD-BaF_2 process. This paper represents the case when too much liquid is allowed to form early in the process and a clearly defined bimodal structure develops that is uniformly found throughout the sample. While the J_c values obtained in these films are high, they will not allow for an overall wire performance that exceeds existing Bi-2223 wire technology unless the YBCO films are thicker than 3 μm.[46]

To obtain a through-thickness, uniform microstructure or to tailor the microstructure to maximize J_c, CuO segregation and liquid phase formation must be controlled during the conversion process. Recently, the authors have reported on improvements in the processing that appear to limit the detrimental effects of too much liquid phase formation.[53] These improvements include modifications to the precursor layer, enabling the elimination of the nucleation step. A detailed discussion of the process changes is covered elsewhere.[54] However, when the microstructures were analyzed, localized areas could be found that contained the essential elements of the bimodal structure, namely, large grains of YBCO with Y_2O_3 precipitates, layers of the Ba-containing secondary phases, and small pockets of YBCO grains containing small angle tilts like those shown in Figs. 3(d) and 3(e). Thus, the results presented in this paper provide a baseline for interpreting microstructures in the higher J_c

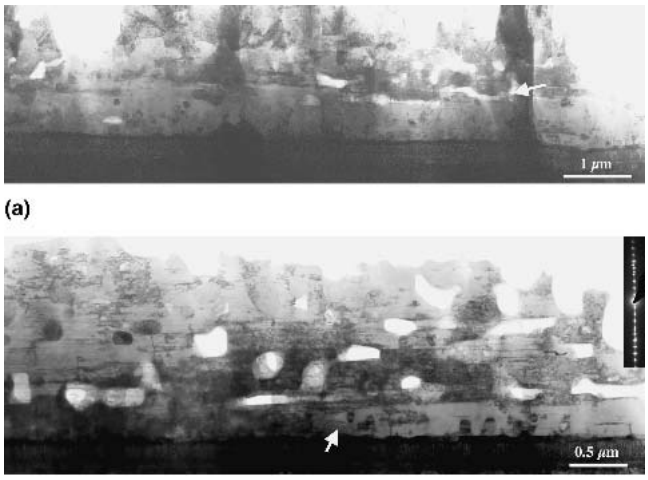

FIG. 15. TEM cross-sectional images of 1.4-μm and 1.8-μm RABiTS samples that had no surface irregularities like those shown in Fig. 3. Very few second-phase layers were found in these samples. (a) TEM shows a region of the 1.4-μm YBCO film that is bimodal, while only part of the structure of the 1.8-μm YBCO film in (b) is bimodal. This data, coupled with Fig. 14, shows that the bimodal structure varies from point-to-point in the films with minimal second phase layers. The arrow in (a) indicates some porosity that lies along the dividing line in the bimodal structure. The arrow in (b) indicates where the large YBCO grain with Y_2O_3 precipitates terminates in the film. The bars at the left of each image denote the interface of the YBCO films with the underlying buffer layers.

BaF_2-based films. It may be difficult to produce a through-thickness uniform microstructure in thick BaF_2 films. As pointed out by Yoshizumi et al., thick BaF_2 YBCO films appear to be more conducive to forming liquid phases during the conversion process, and vestiges of the bimodal structure may always be present.[51] Nevertheless, eliminating or reducing the number of the second phase layers by limiting liquid phase formation during conversion appears to minimize or reverse alignment degradation in the thick BaF_2 films. Higher J_c levels have been found in the absence of the second-phase layers.

V. SUMMARY

The PVD-BaF_2 YBCO films examined in this work were characterized by laminar grain structures that result from the anisotropic growth characteristics of the YBCO phase and its precipitation from a transient liquid phase during the conversion process. Liquid-phase assisted growth of the YBCO was suggested by features of a bimodal microstructure that developed in fully and partially processed films. The bimodal microstructure is defined by large, well-formed YBCO grains with Y_2O_3 precipitates in the bottom region of the film and small YBCO grains with a high density of stacking faults in the upper half. In some cases, the YBCO grain size in the bottom region of the bimodal structure exceeded the 50 μm. $Ba_2Cu_3O_y$ or Ba–O–F/CuO second phase layers were often found between large YBCO grains in the bottom half of the film. Discrete secondary phases of $Y_2Cu_2O_5$, Y_2O_3, $BaCu_2O_y$, and $Ba_2Cu_3O_y$ or Ba–O–F/CuO could also be found among the smaller YBCO grains in the top portion of the bimodal structure. For the series of samples examined in this work, it was found that the dividing line of the bi-modal structure was generally at one half of the film thickness. However, exceptions to this trend were found, and the highest critical current densities (J_c) and best film alignments for a given film thickness were found in the samples where the layers of $Ba_2Cu_3O_y$ or Ba–O–F/CuO were minimized or eliminated from the films. These latter films also had incomplete bimodal structures in that the bimodal structure was found to vary from point-to-point within the films. Liquid phases are part of the conversion process of BaF_2-based YBCO films. The microstructures presented here provide a baseline for interpreting the role of liquids in the phase formation of other YBCO films made by the BaF_2-process.

ACKNOWLEDGMENTS

This work was performed under the auspices of the United States Department of Energy (DOE), Office of Electric Transmission and Distribution, as part of a DOE program to develop electric power technology, under contract W-7405-ENG-36.

REFERENCES

1. A.P. Malozemoff, S. Annavarapu, L.G. Fritzemeier, Q. Li, V. Prunier, M.W. Rupich, C. Thieme, W. Zhang, A. Goyal, M. Paranthaman, and D.F. Lee: Low-cost YBCO coated conductor technology. *Supercond. Sci. Technol.* **13,** 473 (2000).
2. Y. Iijima, N. Tanabe, O. Kohno, and Y. Ikeno: In-plane aligned $YBa_2Cu_3O_{7-x}$ thin films deposited on polycrystalline metallic substrates. *Appl. Phys. Lett.* **60,** 769 (1992).
3. R.P. Reade, P. Berdahl, R.E. Russo, and S.M. Garrison: Laser deposition of biaxially textured yttria-stabilized zirconia buffer layers on polycrystalline metallic alloys for high critical current Y–Ba–Cu–O thin films. *Appl. Phys. Lett.* **61,** 2231 (1992).
4. X.D. Wu, S.R. Foltyn, P. Arendt, J. Townsend, C. Adams, I.H. Campbell, P. Tiwari, Y. Coulter, and D.E. Peterson: High current $YBa_2Cu_3O_{7-\partial}$ thick films on flexible nickel substrates with textured buffer layers. *Appl. Phys. Lett.* **65,** 1961 (1994).
5. K. Hasegawa, K. Fujino, H. Mukai, M. Konishi, K. Hayashik, K. Sata, S. Honjo, Y. Sato, H. Ishii, and Y. Iwata: Biaxially aligned YBCO film tapes fabricated by all pulsed laser deposition. *Appl. Supercond.* **4,** 487 (1998).
6. M. Bauer, R. Semerad, and H. Kinder: YBCO films on metal substrates with biaxially aligned MgO buffer layers. *IEEE Trans. Appl. Supercond.* **9,** 1502 (1999).
7. A. Goyal, D.P. Norton, J.D. Budai, M. Paranthaman, E.D. Specht, D.M. Kroeger, D.K. Christen, Q. He, B. Saffian, F.A. List, D.F. Lee, P.M. Martin, C.E. Klabunde, E. Hartfield, and V.K. Sikka: High critical current density superconducting tapes by epitaxial deposition of $YBa_2Cu_3O_x$ thick films on biaxially textured metals. *Appl. Phys. Lett.* **69,** 1795 (1996).
8. J.E. Mathis, A. Goyal, D.F. Lee, F.A. List, M. Paranthanman, D.K. Christen, E.D. Specht, D.M. Kroeger, and P.M. Martin: Biaxially textured $YBa_2Cu_3O_{7-\partial}$ conductors on rolling assisted biaxially textured substrates with critical current densities of 2–3 MA/cm^2. *Jpn. J. Appl. Phys.* **37,** L1379 (1998).
9. M.W. Rupich, U. Schoop, D.T. Verebelyi, C. Thieme, W. Zhang, X. Li, T. Kodenkandath, N. Nguyen, E. Siegal, D. Buczek, J. Lynch, M. Jowett, E. Thompson, J-S. Wang, J. Scudiere, A.P. Malozemoff, Q. Li, S. Annavarapu, S. Cui, L. Fritzemeier, B. Aldrich, C. Craven, F. Niu, R. Schwall, A. Goyal, and M. Paranthaman: YBCO-coated conductors by an MOD/RABiTS process. *IEEE Trans. Appl. Supercond.* **13,** 2458 (2003).
10. D.P. Norton, A. Goyal, J.D. Budai, D.K. Christen, D.M. Kroeger, E.D. Specht, Q. He, B. Saffian, M. Paranthaman, C.E. Klabunde, D.F. Lee, B.C. Sales, and F.A. List: Epitaxial $YBa_2Cu_3O_7$ on biaxially textured nickel (001): An approach to superconducting tapes with high critical current density. *Science* **274,** 755 (1996).
11. D. Dimos, P. Chaudhari, J. Mannhart, and F.K. LeGoues: Orientation dependence of grain-boundary critical currents in $YBa_2Cu_3O_{7-\delta}$ bicrystals. *Phys. Rev. Lett.* **61,** 219 (1988).
12. N.F. Heining, R.D. Redwing, I. Fei Tsu, A. Gurevich, J.E. Nordman, S.E. Babcock, and D.C. Larbalestier: Evidence for channel conduction in low misorientation angle [001] tilt $YBa_2Cu_3O_{7-x}$ bicrystal films. *Appl. Phys. Lett.* **69,** 577 (1996).
13. D.T. Verebelyi, C. Cantoni, J.D. Budai, D.K. Christen, H.J. Kim, and J.R. Thompson: Critical current density of $YBa_2Cu_3O_{7-\delta}$ low-angle grain boundaries in self-field. *Appl. Phys. Lett.* **78,** 2031 (2001).
14. A.P. Malozemoff, D.T. Verebelyi, S. Fleshler, D. Aized, and D. Yu: HTS wire: Status and prospects. *Physica C* **386,** 424 (2003).
15. A. Gupta, R. Jagannathan, E.I. Cooper, E.A. Giess, J.I. Landman, and B.W. Hussey: Superconducting oxide films with high transition temperature prepared from metal trifluoroacetate precursors. *Appl. Phys. Lett.* **52,** 2077 (1988).

16. P.C. McIntyre, M.J. Cima, and M.F. Ng: Metalorganic deposition of high- J_c $Ba_2YCu_3O_{7-x}$ thin films from trifluoroacetate precursors onto (100) $SrTiO_3$. *J. Appl. Phys.* **68,** 4183 (1990).
17. R. Feenstra, T.B. Lindemer, J.D. Budai, and M.D. Galloway: Effect of oxygen pressure on the synthesis of $YBa_2Cu_3O_{7-\partial}$ thin films by post-deposition annealing. *J. Appl. Phys.* **69,** 6569 (1991).
18. P.C. McIntyre and M.J. Cima: Heteroepitaxial growth of chemically derived ex situ $Ba_2YCu_3O_{7-x}$ thin films. *J. Mater. Res.* **9,** 2219 (1994).
19. J.A. Smith, M.J. Cima, and N. Sonnenberg: High critical current density thick MOD-derived YBCO films. *IEEE Trans. Appl. Supercond.* **9,** 1531 (1999).
20. V.F. Solovyov, H.J. Wiesmann, L. Wu, M. Suenaga, and R. Feenstra: High-rate deposition of 5 μm thick $YBa_2Cu_3O_7$ films using the BaF_2 ex-situ post annealing process. *IEEE Trans. Appl. Supercond.* **9,** 1467 (1999).
21. Y. Yamada, S. Kim, T. Araki, Y. Takahashi, T. Yuasa, H. Kurosaki, I. Hirabayashi, Y. Iijima, and K. Takeda: Critical current density and related microstructures of TFA-MOD YBCO coated conductors. *Physica C* **357-360,** 1007 (2001).
22. O. Castano, A. Cavallaro, A. Palau, J.C. Gonzalez, M. Rossell, T. Puig, F. Sandiumenge, N. Mestres, S. Pinol, A. Pomar, and X. Obradors: High quality $YBa_2Cu_3O_7$ thin films grown by trifluoroacetates metalorganic deposition. *Supercond. Sci. Technol.* **16,** 45 (2003).
23. X. Li, M.W. Rupich, W. Zhang, N. Nguyen, T. Kodenkandath, U. Schoop, D.T. Verebelyi, C. Thieme, M. Jowett, P.N. Arendt, S.R. Foltyn, T.G. Holesinger, T. Aytug, D.K. Christen, and M.P. Paranthaman: High critical current MOD ex situ YBCO films on RABiTS and MgO-IBAD templates. *Physica C* **390,** 249 (2003).
24. V. Selvamanickam, H.G. Lee, Y. Li, J. Reeves, Y. Qiao, Y.Y. Xie, K. Lenseth, G. Carota, M. Funk, K. Zdun, J. Xie, K. Likes, M. Jones, L. Hope, and D.W. Hazelton: Scale up of high performance Y–Ba–Cu–O coated conductors. *IEEE Trans. Appl. Supercond.* **13,** 2492 (2003).
25. S. Donet, F. Weiss, P. Chaudouet, S. Beauquis, A. Abrutis, H.C. Freyhardt, A. Usokin, D. Selbmann, J. Eickemeyer, C. Jimenez, C.E. Bruzek, and J.M. Saugrain: Reel-to-reel MOCVD for YBCO coated conductors. *IEEE Trans. Appl. Supercond.* **13,** 2524 (2003).
26. S.R. Foltyn, P.N. Arendt, P.C. Dowden, R.F. DePaula, J.R. Groves, J.Y. Coulter, Q. Jia, M.P. Maley, and D.E. Peterson: High- T_c coated conductors—performance of meter-long YBCO/IBAD flexible tapes. *IEEE Trans. Appl. Supercond.* **9,** 1519 (1999).
27. L.S. Peng, W. Wang, W. Jo, T. Ohnishi, A.F. Marshall, R.H. Hammond, M.R. Beasley, E.J. Peterson, and R.E. Ericson: In situ high rate growth of high temperature superconductor tapes. *IEEE Trans. Appl. Supercond.* **11,** 3375 (2001).
28. W. Jo, T. Ohnishi, J.U. Huh, R.H. Hammond, and M.R. Beasley: Thickness dependence of critical currents and depth profiling of transport properties in high rate in-situ grown $YBa_2Cu_3O_{7-x}$ films. *IEEE Trans. Appl. Supercond.* **13,** 2817 (2003).
29. S.R. Foltyn, P.N. Arendt, Q.X. Jia, H. Wang, J.L. MacManus-Driscoll, S. Kreiskott, R.F. DePaula, L. Stan, J.R. Groves, and P.C. Dowden: Strongly coupled critical current density values achieved in $Y_1Ba_2Cu_3O_{7-8}$ coated conductors with near-single-crystal texture. *Appl. Phys. Lett.* **82,** 4519 (2003).
30. R. Wordenweber, E. Hollmann, M. Poltiasev, and H.W. Neumuller: Low-pressure large-area magnetron sputter deposition of $YBa_2Cu_3O_{7-\delta}$ films for industrial applications. *Supercond. Sci. Technol.* **16,** 582 (2003).
31. M. Bauer, R. Semerad, H. Kinder, J. Wiesman, J. Dzik, and H.C. Freyhardt: Large area YBCO films on polycrystalline substrates with very high critical current densities. *IEEE Trans. Appl. Supercond.* **9,** 2244 (1999).
32. P.M. Mankiewich, J.H. Scofield, W.J. Skocpol, R.E. Howard, A.H. Dayem, and E. Good: Reproducible technique for fabrication of thin films of high transistion temperature superconductors. *Appl. Phys. Lett.* **51,** 1753 (1987).
33. T. Izumi, T. Honjo, Y. Tokunaga, H. Fuji, R. Teranishi, Y. Iijima, T. Saitoh, Y. Nakamura, and Y. Shiohara: High- J_c YBCO coated conductors by metal organic deposition method using trifluoroacetates. *IEEE Trans. Appl. Supercond.* **13,** 2500 (2003).
34. P.C. McIntyre, M.J. Cima, J.A. Smith, R.B. Hallock, M.P. Siegal, and J.M. Phillips: Effect of growth conditions on the properties and morphology of chemically derived epitaxial thin films of $Ba_2YCu_3O_{7-x}$ on (001) $LaAlO_3$. *J. Appl. Phys.* **71,** 1868 (1992).
35. L. Wu, Y. Zhu, V.F. Solovyov, H.J. Wiesmann, A.R. Moodenbaugh, R.L. Sabatini, and M. Suenaga: Nucleation and growth of $YBa_2Cu_3O_x$ on $SrTiO_3$ and CeO_2 by a BaF_2 postdeposition reaction process. *J. Mater. Res.* **16,** 2869 (2001).
36. J. Shibata, T. Honjo, H. Fuji, T. Araki, I. Hirabayashi, T. Hirayama, T. Izumi, Y. Shiohara, T. Yamamoto, and Y. Ikuhara: Cyrstallization mechanism of $Nd_{1+x}Ba_{2-x}Cu_3O_{7-y}$ and $YBa_2Cu_3O_{7-y}$ films deposited by metalorganic deposition method using trifluoroacetates. *J. Mater. Res.* **17,** 1266 (2002).
37. V.F. Solovyov, H.J. Wiesmann, and M. Suenaga: Growth rate limiting mechanisms of $YBa_2Cu_3O_7$ films manufactured by ex situ processing. *Physica C* **353,** 14 (2001).
38. T. Honjo, Y. Nakamura, R. Teranishi, H. Fuji, J. Shibata, T. Izumi, and Y. Shiohara: Growth mechanism of YBCO films in metal organic deposition method using trifluoroacetates. *IEEE Trans. Appl. Supercond.* **13,** 2516 (2003).
39. D.M. Feldmann, D.C. Larbalestier, R. Feenstra, A.A. Gapud, J.D. Budai, T.G. Holesinger, and P.N. Arendt: Through-thickness superconducting and normal-state transport properties revealed by thinning of thick film ex situ $YBa_2Cu_3O_{7-x}$ coated conductors. *Appl. Phys. Lett.* **83,** 3951 (2003).
40. O. Castano, A. Cavallaro, A. Palau, J.C. Gonzalez, M. Rosell, T. Puig, S. Pinol, N. Mestres, F. Sandiumenge, A. Pomar, and X. Obradors: Influence of porosity on the critical currents of trifluoroacetate-MOD $YBa_2Cu_3O_7$ films. *IEEE Trans. Appl. Supercond.* **13,** 2504 (2003).
41. R. Feenstra (unpublished).
42. P.N. Arendt, S.R. Foltyn, J.R. Groves, R.F. Depaula, P.C. Dowden, J.M. Roper, and J.Y. Coulter: YBCO/YSZ coated conductors on flexible Ni alloy substrates. *Appl. Supercond.* **4,** 429 (1996).
43. C. Cantoni, D.K. Christen, R. Feenstra, A. Goyal, G.W. Ownby, D.M. Zehner, and D.P. Norton: Reflection high-energy electron diffraction studies of epitaxial oxide seed-layer growth on rolling-assisted biaxially textured substrate Ni(001): The role of surface structure and chemistry. *Appl. Phys. Lett.* **79,** 3077 (2001).
44. G. Cliff and G.W. Lorimer: Quantitative analysis of thin specimens. *J. Microsc.* **103,** 203 (1975).
45. E.D. Specht, A. Goyal, D.F. Lee, F.A. List, D.M. Kroeger, M. Paranthaman, R.K. Williams, and D.K. Christen: Cube-textured nickel substrates for high-temperature superconductors. *Supercond. Sci. Technol.* **11,** 945 (1998).
46. A.P. Malozemoff, private communication (2004).
47. T.G. Holesinger, S.R. Foltyn, P.N. Arendt, H. Kung, Q.X. Jia, R.M. Dickerson, P.C. Dowden, R.F. DePaula, and J.Y. Coulter: The microstructure of continously processed $YBa_2Cu_3O_y$ coated conductors with underlying CeO_2 and IBAD YSZ Buffer Layers. *J. Mater. Res.* **15,** 222 (2000).
48. T.A. Vanderah, R.S. Roth, and H.F. McMurdie: *Phase Diagrams for High T_c Superconductors II*, 1st ed. (The American Ceramic Society, Westerville, OH, 1997), p. 278.
49. U. Scotti di Uccio, F.M. Granzozio, A. Di Chiara, F. Tafuri, O.I. Lebedev, K. Verbist, and G. Van Tendeloo: Phase competi-

tion between Y_2BaCuO_5 and Y_2O_3 precipitates in Y-rich YBCO thin films. *Physica C* **321,** 162 (1999).
50. W. Jo, L.S-J. Peng, W. Wang, T. Ohnishi, A.F. Marshall, R.H. Hammond, M.R. Beasley, and E.J. Peterson: Thermodynamic stability and kinetics of Y–Ba–Cu–O film growth at high rates in atomic and molecular oxygen. *J. Cryst. Growth* **225,** 183 (2001).
51. M. Yoshizumi, I. Seleznev, and M.J. Cima: Reactions of oxyfluoride precursors for the preparation of barium yttrium cuprate films. *Physica C* **403,** 191 (2004).
52. W. Wong-Ng, L.P. Cook, J. Suh, I. Levin, M. Vaudin, R. Feenstra, and J.P. Cline: Phase relationships and phase formation in the system BaF_2–BaO–Y_2O_3–CuO_x–H_2O, in *Materials for High-Temperature Superconductor Technologies*, edited by M.P. Paranthaman, M.W. Rupich, K. Salama, J. Mannhart, and T. Hasegawa (Mater. Res. Soc. Symp. Proc. **689,** Warrendale, PA, 2002), p. 337.
53. T.G. Holesinger, D.M. Feldmann, and R. Feenstra: Development of Ex-situ processed, high-I_c coated conductors, Superconductivity for Electric Systems 2004 Annual Peer Review, Washington, D.C., 2004.
54. R. Feenstra, A.A. Gapud, F.A. List, E.D. Specht, D.K. Christen, T.G. Holesinger and D. M. Feldmann: Critical currents I_c(77K) > 350 A/cm-width achieved in ex situ YBCO coated conductors using a faster conversion process, *IEEE Trans. Appl. Supercond.* (2004, in press).